Eq. (4.8) is solved in cylindrical coordinates with boundary conditions, Eqs. (4.9), (4.10), and (4.11), resulting in

$$\phi_n(\vec{r}) = J_m\left(\frac{\pi\alpha_{mn}}{a} r\right) \begin{matrix}\sin\\ \cos\end{matrix} (m\theta) \cos\left[(\ell + \tfrac{1}{2}) \frac{\pi}{L} z\right] \tag{4.12}$$

where n represents the quantum number trio ℓ,m,n which has integer values equal to 0,1,2, ... The eigenfunctions ϕ_n satisfy the orthonormal condition

$$\int \phi_m(\vec{r})\, \phi_n(\vec{r})\, dV = V\Lambda_n\, \delta_{mn} \tag{4.13}$$

where δ_{mn} is the Kronecker delta. The normalization constant Λ_n is given by

$$V\Lambda_n \equiv V\Lambda_{n,m} = \frac{\pi a^2 L}{2\varepsilon_m} \left[1-\left(\frac{m}{\pi\alpha_{mn}}\right)^2\right] J_m^2(\pi\alpha_{mn}), \tag{4.14}$$

where $\varepsilon_m = 2(1+\delta_{om})^{-1}$. The eigenvalue α_{mn} is defined by

$$J_m'(\pi\alpha_{mn}) = 0, \tag{4.15}$$

where J_m' is the derivative of J_m with respect to its argument. A few values of α_{mn} are

$$\begin{matrix} \alpha_{00} = 0.0000 & \alpha_{01} = 1.2197 & \alpha_{02} = 2.2331 & \cdots \\ \alpha_{10} = 0.5861 & \alpha_{11} = 1.6970 & \alpha_{12} = 2.7140 & \cdots \\ \alpha_{20} = 0.9722 & \alpha_{21} = 2.1346 & \alpha_{22} = 3.1734 & \cdots \\ \end{matrix} \tag{4.16}$$

$$\alpha_{mn} \rightarrow n + \tfrac{1}{2}m - \tfrac{3}{4} \qquad m < n >> 1.$$

MOTHER E 332

8010210334

$$\text{At } r = b \qquad \frac{\partial \phi_n}{\partial r} = 0 \qquad \text{(rigid inner wall)} \tag{4.24}$$

$$\text{At } z = 0 \qquad \frac{\partial \phi_n}{\partial z} = 0 \qquad \text{(rigid bottom)} \tag{4.25}$$

$$\text{At } z = L \qquad \phi \text{ [illegible]} \qquad \text{(water surface).} \tag{4.26}$$

Equation (4.22) is solved [illegible]drical coordinates with boundary conditions, Eqs. (4.23), ([illegible].25), and (4.26), resulting in

$$\phi_n(\vec{r}) = \zeta_{mn}(r) \begin{matrix}\sin\\ \cos\end{matrix} (m\theta) \cos[(\ell + \tfrac{1}{2}) \tfrac{\pi}{L} z] \tag{4.27}$$

where, as before, n represents the quantum number trio ℓ,m,n which has integer values equal to 0,1,2, ... The eigenfunctions ϕ_n satisfy Eq. (4.13) which determines the normalization constant $V\Lambda_n$ (see Eq. (4.13)). The radial function $\zeta_{mn}(r)$ is

$$\zeta_{mn}(r) = J_m(\frac{\pi\gamma_{mn} r}{a}) - \frac{J'_m(\pi\gamma_{mn} b/a)}{N'_m(\pi\gamma_{mn} b/a)} N_m(\frac{\pi\gamma_{mn} r}{a}), \tag{4.28}$$

where the eigenvalues $\pi\gamma_{mn}$ are defined by the roots of

$$J'_m(\pi\gamma_{mn}) N'_m(\pi\gamma_{mn} b/a) - J'_m(\pi\gamma_{mn} b/a) N'_m(\pi\gamma_{mn}) = 0 \quad , \tag{4.29}$$

J'_m and N'_m being the derivatives of J_m and N_m with respect to their arguments. The roots of Eq. (4.29) are also available in the literature[28].

For multiple sources of strength $S_j(t_o)$ located at coordinates (r_j, θ_j, z_j), the source distribution function becomes

$$q(\vec{r}_o, t_o) = \rho \sum_j S_j(t_o) \frac{1}{r} \delta(r_o - r_j) \delta(\theta_o - \theta_j) \delta(z_o - z_j), \tag{4.30}$$

where

$$S_j(t_o) = S_o(t_o - t_j)\, u(t_o - t_j) \quad , \tag{4.31}$$

u(t) is the unit step function, and t_j is the initiation time of the j^{th} source. The source function $S_o(t)$ is the Mark II chugging source derived from the 4T chugging source and assumed to occur at each vent exit.

Eq. (4.30), together with the Fourier transform of Eq. (4.7), are inserted into Eq. (4.5), resulting in

$$p(\vec{r},t) = 4\pi\rho c^2 \sum_n \frac{\Omega_n(\vec{r})}{\omega_n V\Lambda_n} \sum_j \Omega_n(\vec{r}_j) \int_o^{t^+} S_j(t_o) \sin[\omega_n(t-t_o)]\, dt_o, \tag{4.32}$$

where

$$\Omega_n(\vec{r}) = \zeta_{mn}(\vec{r}) \cos[(\ell + \tfrac{1}{2})\, \tfrac{\pi}{L}\, z] \tag{4.33}$$

$$\Omega_n(\vec{r}_j) = \zeta_{mn}(r_j) \cos[m(\theta - \theta_j)] \quad \cos[(\ell + \tfrac{1}{2})\, \tfrac{\pi}{L}\, z_j] \tag{4.34}$$

$$V\Lambda_n = \frac{\pi a^2 L}{2\, \varepsilon_m} [\zeta^2_{mn}(a) - (\tfrac{b}{a})^2 \zeta^2_{mn}(b) - (\tfrac{m}{\pi\gamma_{mn}})^2 \{\zeta^2_{mn}(a) - \zeta^2_{mn}(b)\}] \ . \tag{4.35}$$

$$(\frac{\omega_n}{c})^2 = (\frac{\pi\gamma_{mn}}{a})^2 + (\ell + \tfrac{1}{2})^2\ (\tfrac{\pi}{L})^2. \tag{4.36}$$

Eq. (4.32) is evaluated numerically by the code IWEGS/MARS. Note that the roots of Eq. (4.29) are dependent on the containment diameter ratio b/a. Thus, the natural frequencies predicted by Eq. (4.36) will be different for each of the Mark II containments. Table 4-1 lists the five lowest frequencies for the Susquehanna containment. Notice that the first transverse mode has a frequency only 7 Hz greater than the fundamental.

Table 4-1

SUSQUEHANNA SUPPRESSION POOL NATURAL FREQUENCIES

ℓ m $n^{(2)}$	Transverse Root, ($\pi\gamma_{mn}$)	Frequency, $Hz^{(1)}$ ($f_{\ell mn}$)	Mode
0 0 0	0.	54.35	fundamental
0 1 0	1.54512	61.12	1st tangential
0 2 0	2.93655	76.02	2nd tangential
0 3 0	4.16609	92.96	3rd tangential
0 0 1	4.88471	103.79	1st radial

Note (1): Solving Equation (4.29) with the following parameters:

$c = 1524$ m/s (5000 ft/s)

$a = 13.4$ m (43.96 ft)

$b = 4.42$ m (14.5 ft)

$L = 7.01$ m (23.0 ft)

Note (2): m index corresponds to azimuthal direction

n index corresponds to radial direction

ℓ index corresponds to axial direction

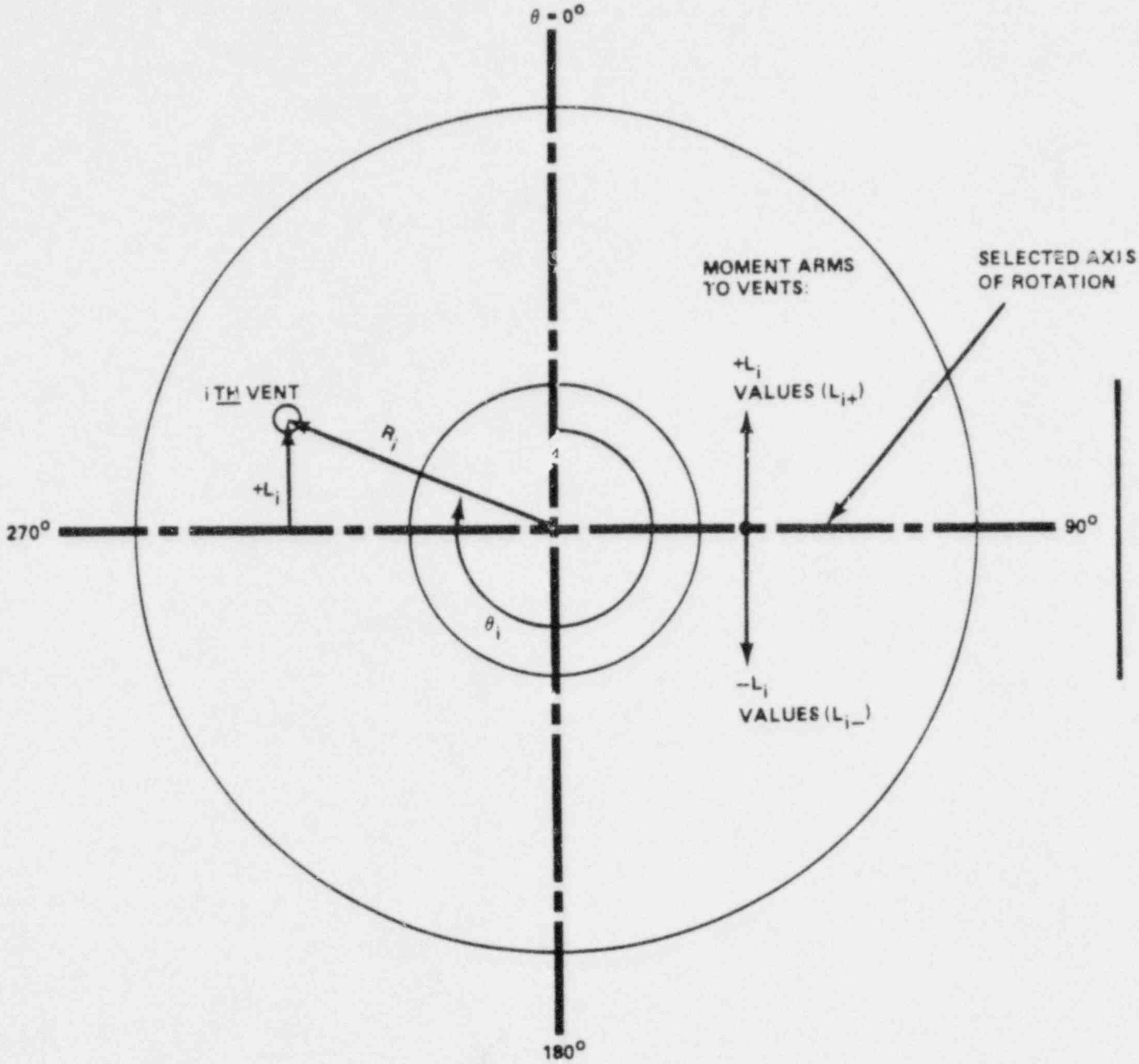

Figure 7-13 Arrangement of Values for L_i or R_i and Θ_i

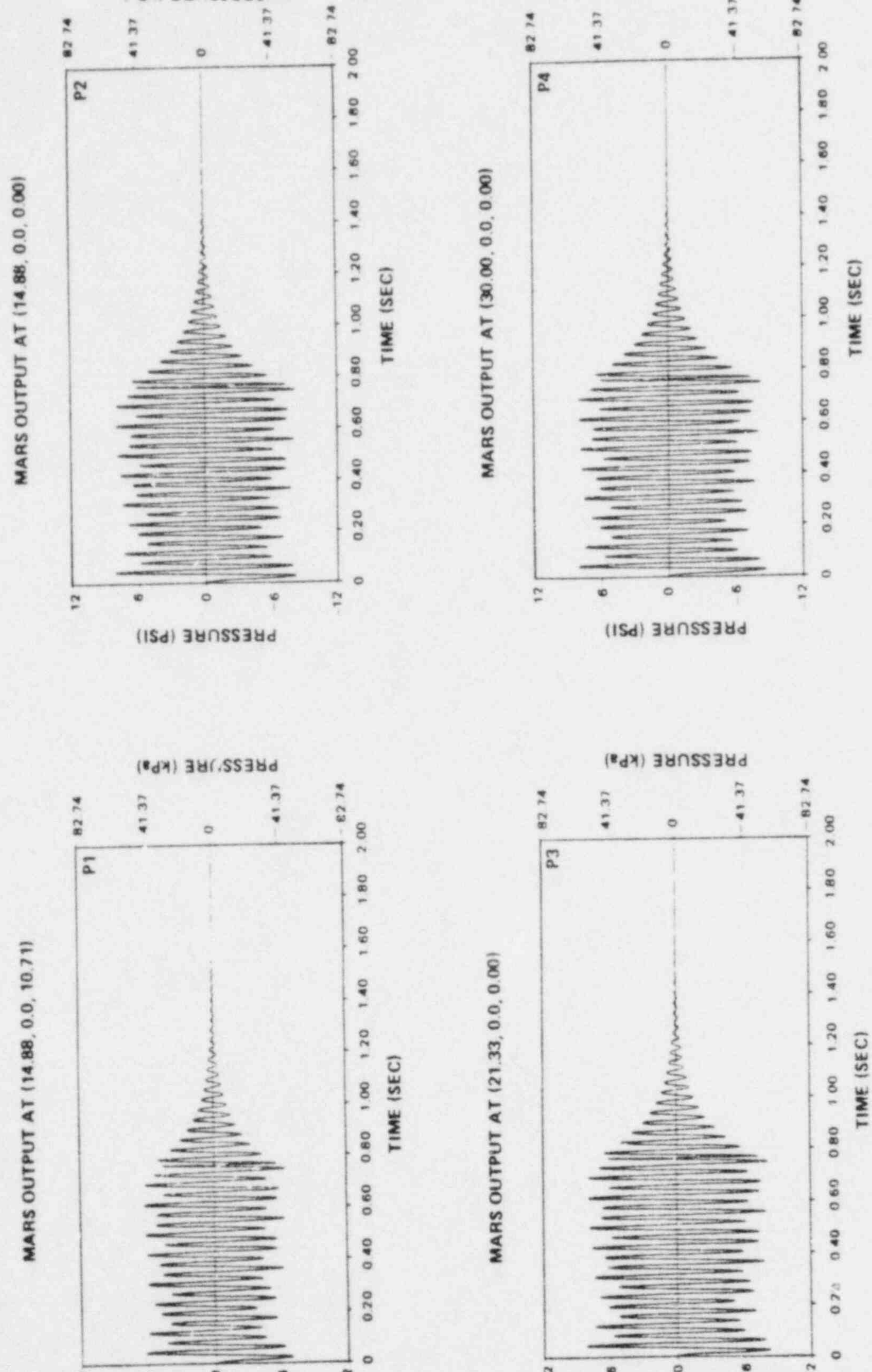

Figure 8-5 Flexible Wall Pressure Time Histories at $\theta = 0^o$ - Symmetric Load Case
(See Fig. 8-4 for Location of Points)

G10028209

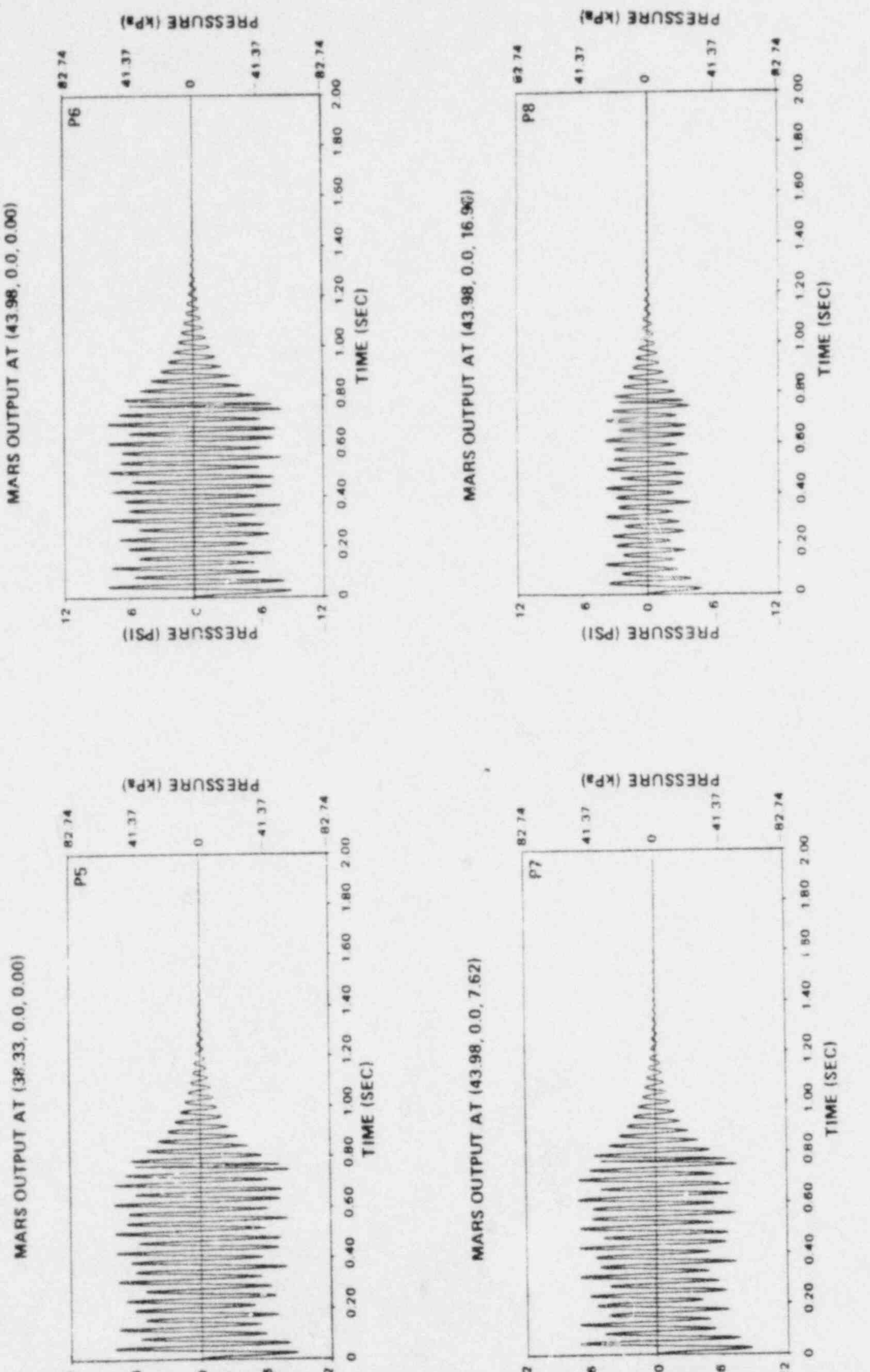

Figure 8-6 Flexible Wall Pressure Time-Histories at $\theta = 0^{o}$ - Symmetric Load Case
(See Fig. 8-4 for Location of Points)

G1002823 116

Errata 1

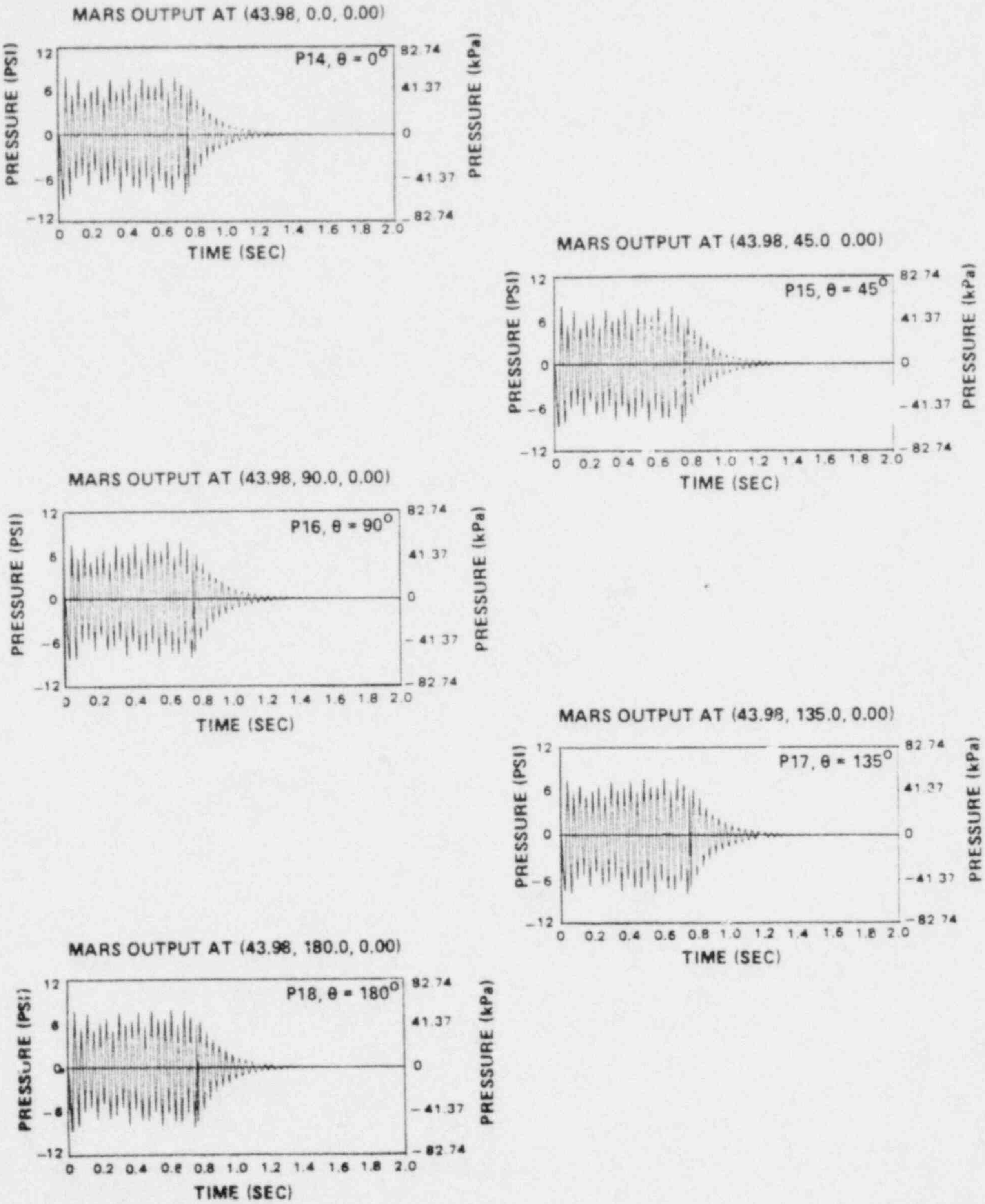

Figure 8-7 Flexible Wall Pressure Time-Histories or Containment Wall at Basemat - Symmetric Load Case (Refer to Fig. 8-3 for Location of Points)

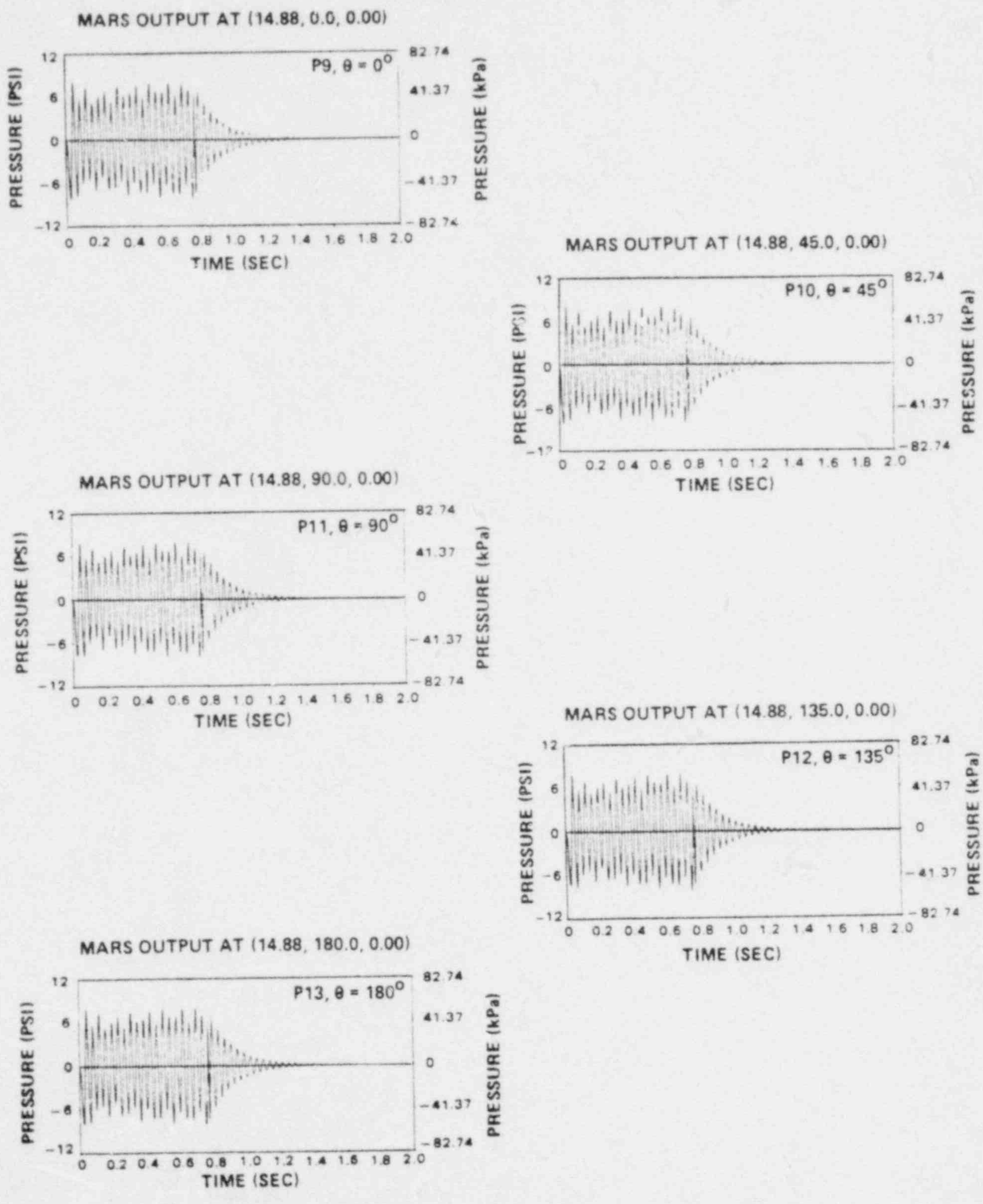

Figure 8-8 Flexible Wall Pressure Time-Histories on Pedestal at Basemat - Symmetric Load Case (Refer to Fig. 8-3 for Location of Points)

be zero. A spectral analysis of a typical flexible wall pressure time-history is shown in Fig. 8-9. Contribution from the pool axial fundamental at 25 Hz can be seen along with a contribution from the vent fundamental at 10 Hz.

Asymmetric load case results can be seen in Fig. 8-10 where flexible wall pressures at the intersection of the containment wall and basemat at 0° and 180° are shown. The pressure time-history at 0° is in the middle of the "high side" of the pool where the design source strength has been multiplied by $(1 + \alpha)$. The pressure time-history at 180° is in the middle of the "low side" of the pool where the design source has been multiplied by $(1 - \alpha)$. These two traces show that the limit of the asymmetry in the asymmetric chugging load is less than 20 kPa (3 psi). A comparison of the asymmetric load case peak overpressure and peak underpressure with the bounding load specification is shown in Fig. 8-11.

The symmetric load case flexible wall pressure field was then applied to the Mark II containment structural model shown in Fig. 8-12. This structural model is an ANSYS finite element model of a typical reinforced concrete Mark II containment. Flat shell elements are used to model the reinforced concrete containment structure and the reactor vessel. Pipe elements are used to model the columns supporting the drywell floor. The ANSYS program uses stiffness-proportional-damping. A damping value corresponding to a structural modal damping value of approximately 4% was used.

Acceleration response spectra for various important nodes in the containment are shown in Figs. 8-13 through 8-17. Results for the improved chugging load (shown as solid lines) are compared to the Dynamic Forcing Function Information Report (DFFR) bounding load (dashed lines). The four curves shown for each load definition correspond to spectral damping values of 0.5%, 1.0%, 2.0%, and 5.0%. The improved chugging load acceleration response spectra peaks are generally lower or comparable to the bounding load except in the vicinity of the reactor pressure vessel (RPV).

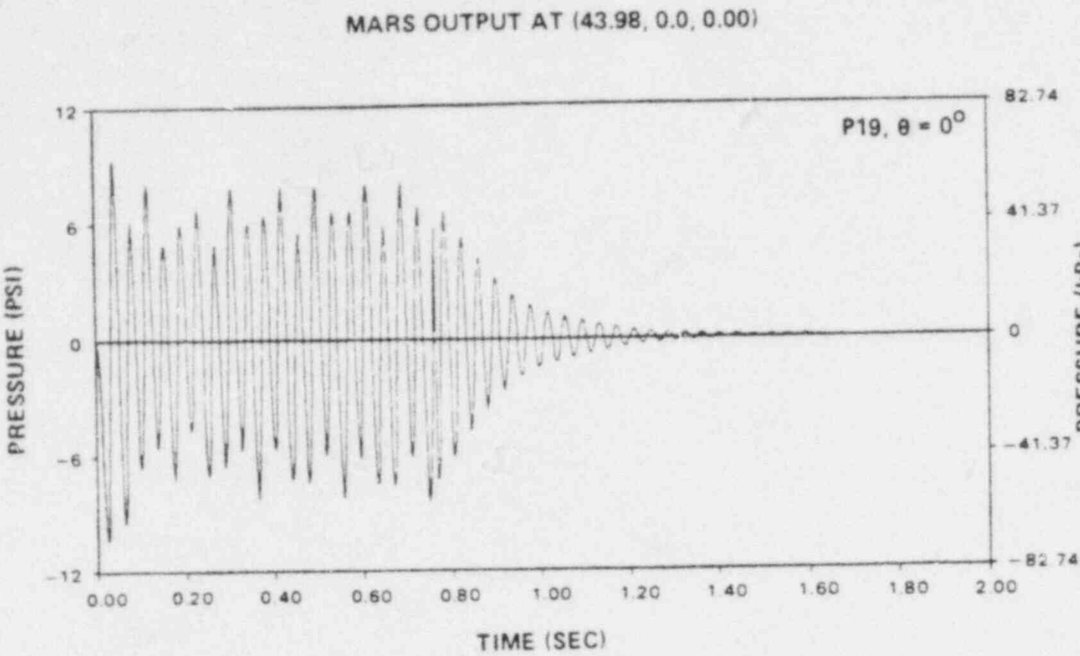

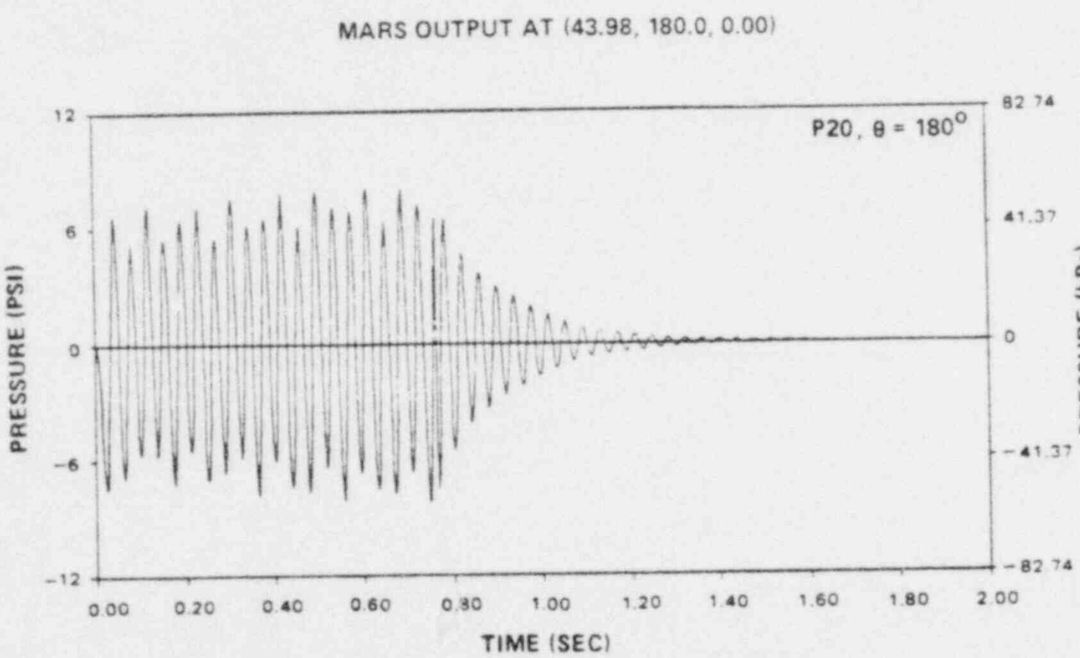

Figure 8-10 Flexible Wall Pressures at Basemat and Containment Wall - Asymmetric Load Case

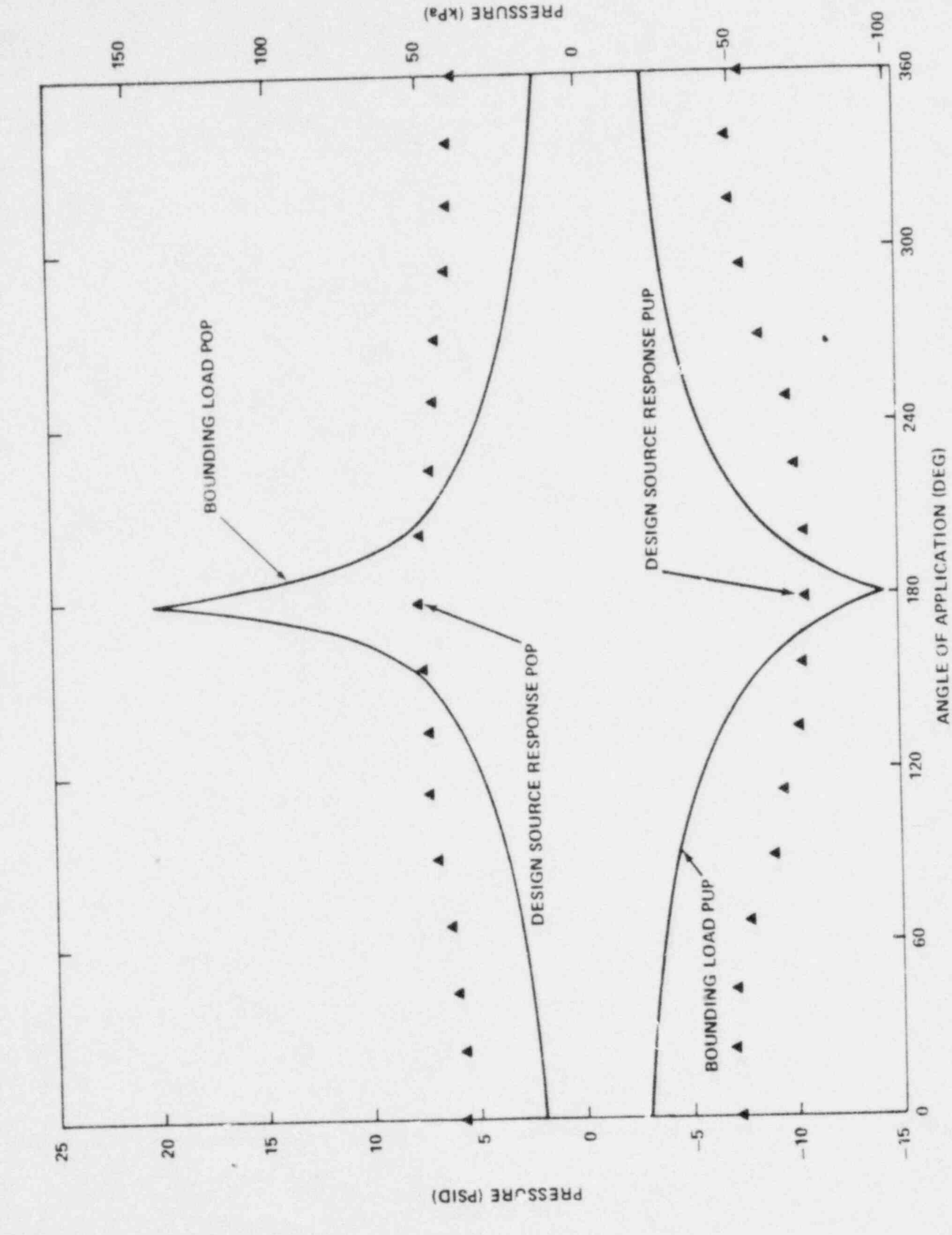

Figure 8-11 Chugging Load Profile - Asymmetric Load Case

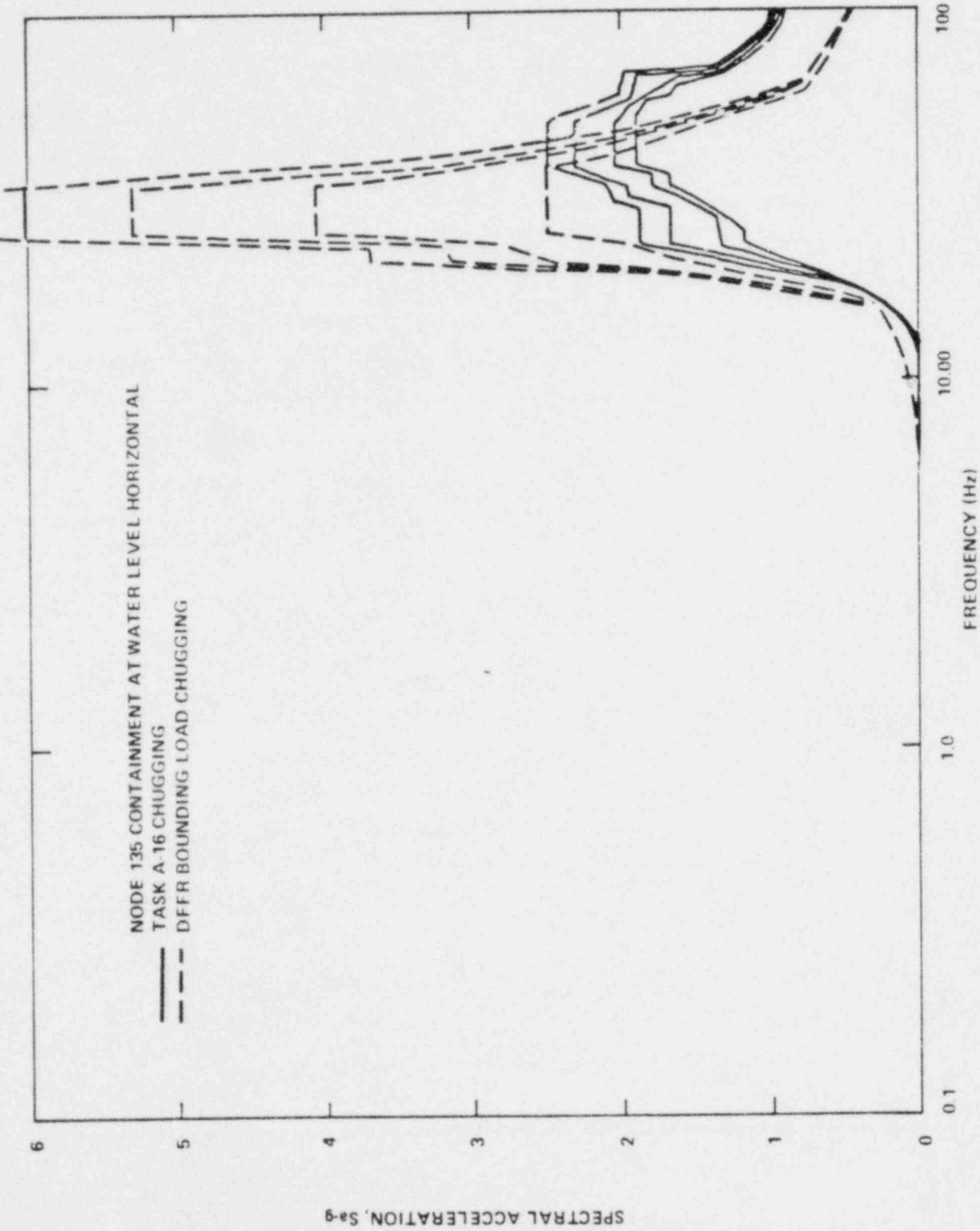

Figure 8.13 Mark II Containment Acceleration Response Spectrum

G1002820 106

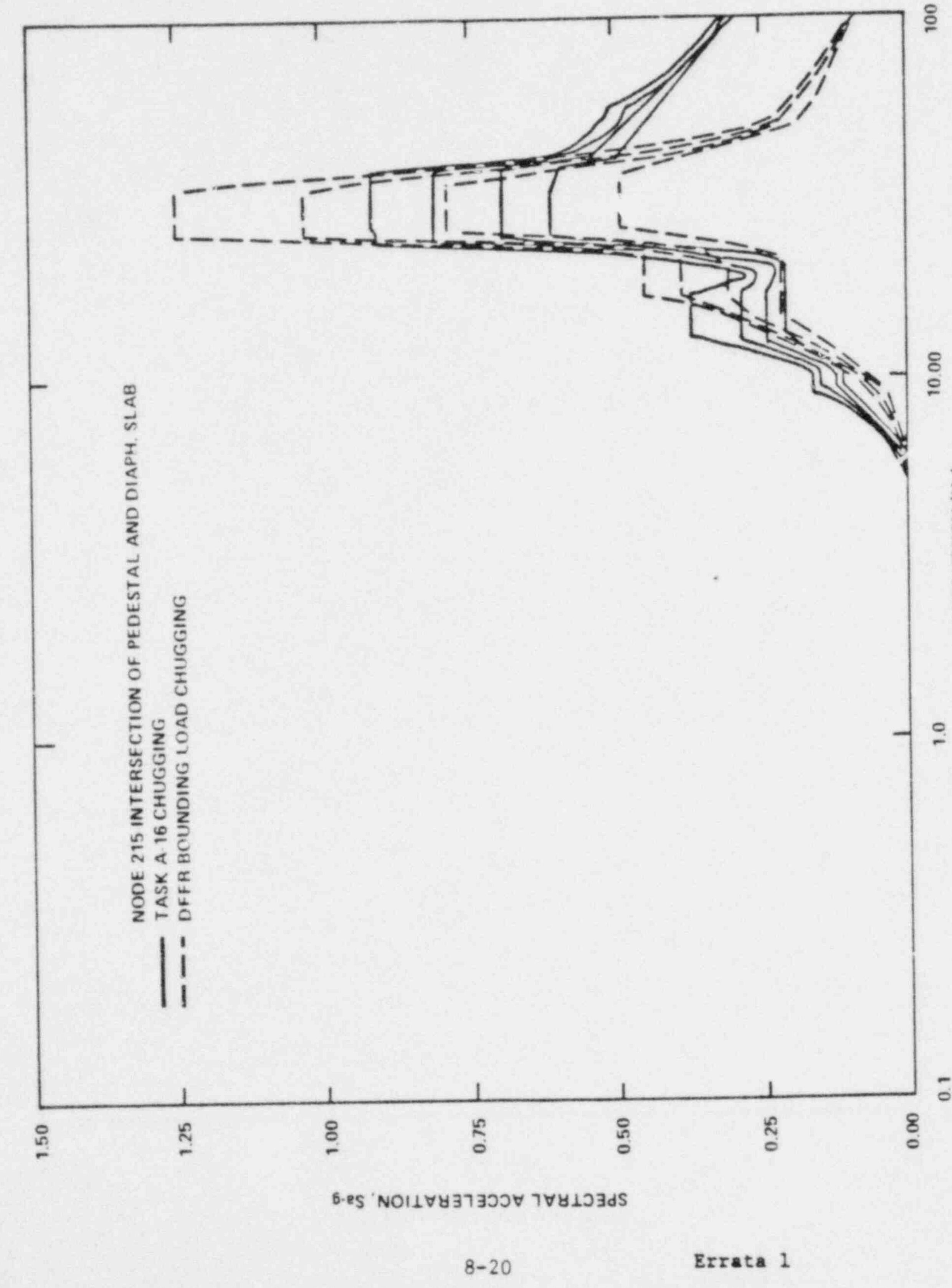

Figure 8-14 Mark II Containment Acceleration Response Spectrum

Errata 1

G1002820.107

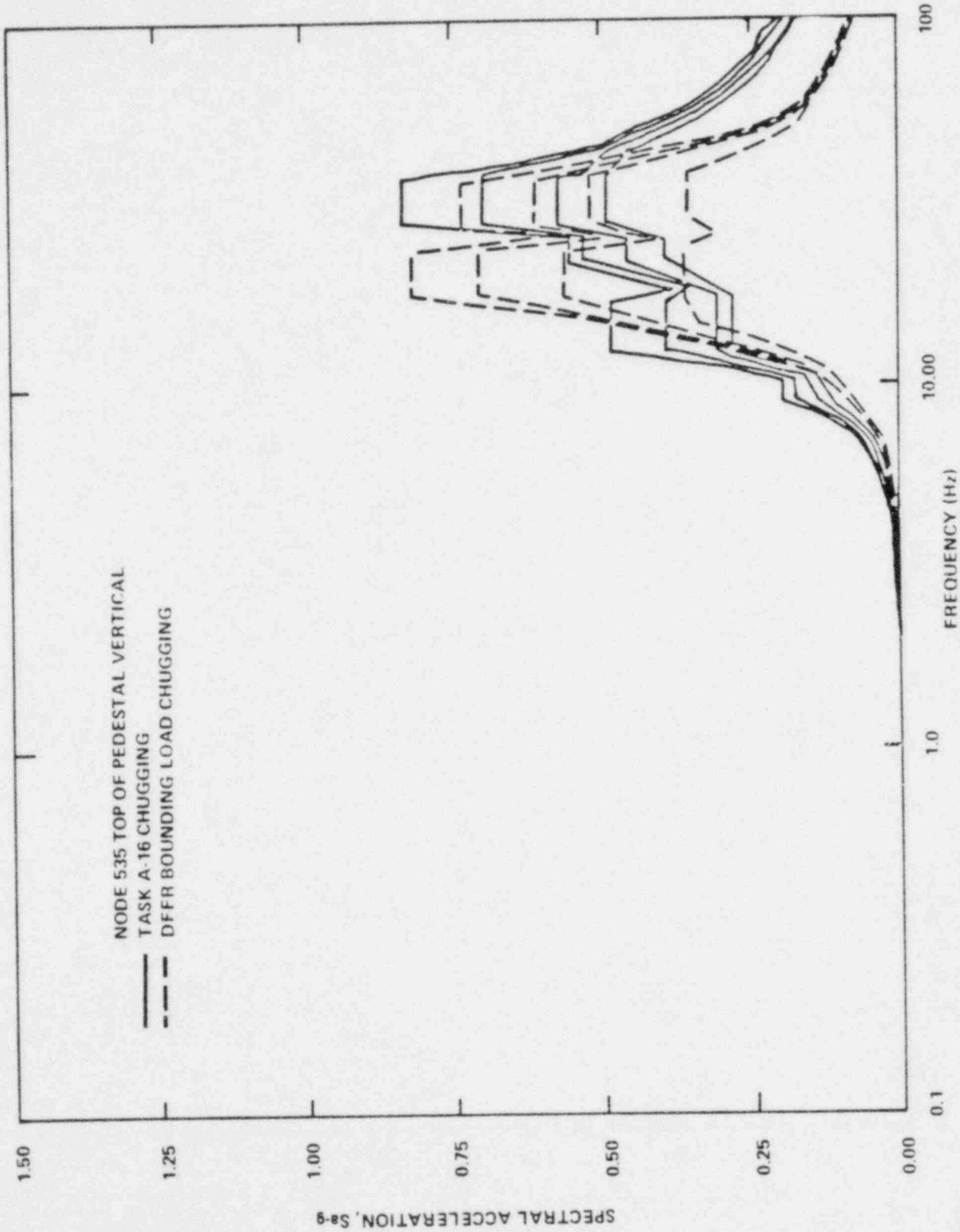

Figure 8-15 Mark II Containment Acceleration Response Spectrum

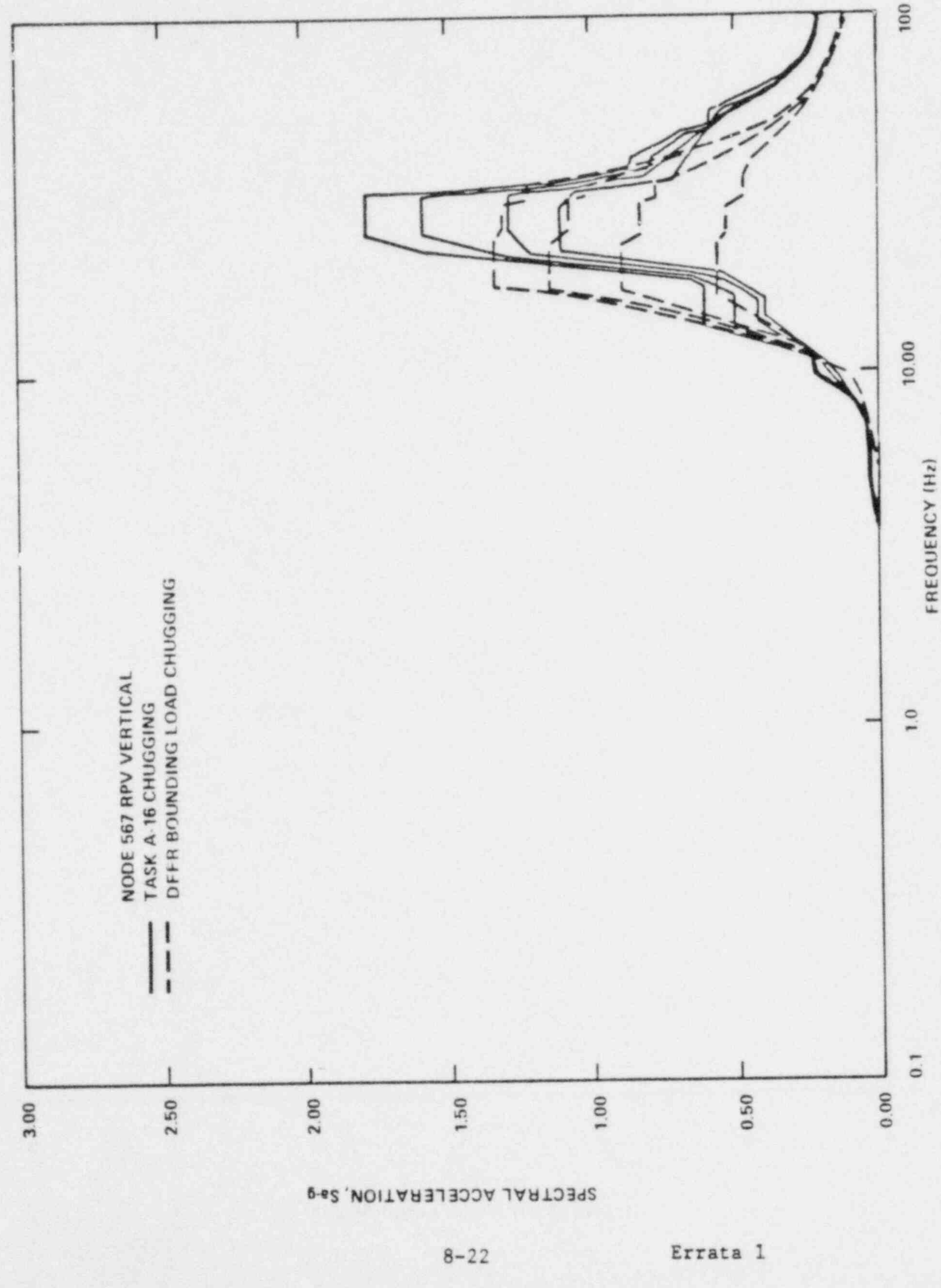

Figure 8-16 Mark II Containment Acceleration Response Spectrum

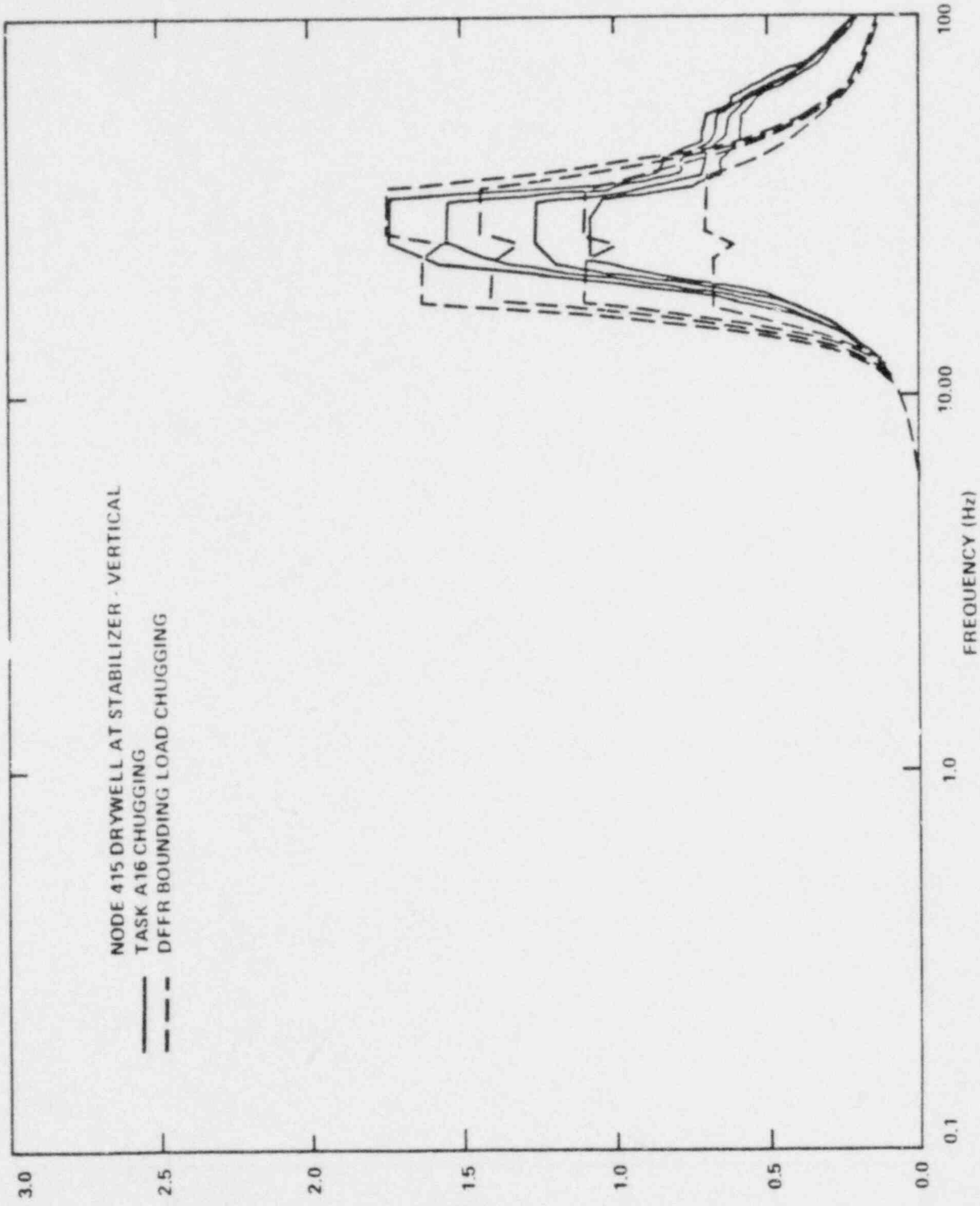

Figure 8-17 Mark II Containment Acceleration Response Spectrum

η	Bulk viscosity (3.6)
η_N	Rigid wall wave number (5.12)
θ	Azimuth angle
θ_o	Azimuth angle of source in 4T (4.19)
θ_j	Azimuth angle of jth source in Mark II (4.30)
κ	Thermal conductivity
λ_N	Fluid damping constant (5.6), (5.36)
$\Lambda_n(\omega)$	Eigenfunction mean square amplitude (4.13)
$\Lambda_N^o(\omega)$	Rigid wall eigenfunction mean square amplitude (5.14)
$\Lambda(x)$	Triangular impulse function (3.3)
μ	Coefficient of shear viscosity (3.6)
μ	Poisson's ratio
$\xi(\omega,\vec{r}_s)$	Specific acoustic conductance (see page 5-6)
$\bar{\xi}(\omega)$	Spatial average specific acoustic conductance (see page 5-13), (5.33)
ρ	Mean fluid density
ρ_s	Mean boundary density

$\sigma(\omega,\vec{r}_s)$	Specific acoustic susceptance (see page 5-6)
$\bar{\sigma}(\omega)$	Spatial average specific acoustic susceptance (see page 5-13), (5.34)
$\vec{\tau}$	Viscous-stress tensor (3.7)
τ	Impulse duration
$\phi_n(\vec{r})$	Rigid wall eigenfunction (4.8), (4.12), (4.27)
Φ	Potential energy per unit mass (3.6)
$\Psi_n(\omega,\vec{r})$	Flexible wall eigenfuntion (5.3), (5.24), (5.25)
ω_n	Flexible wall eigenfrequency (5.6), (5.27), (5.35), (5.41)
$\omega_n^o \equiv c\eta_n$	Rigid wall eigenfrequency (5.27)
ω_b	4T base plate vibrational frequency (5.41), (Table 5-1)
ω_s	Structure vibrational frequency (5.29), (5.35)
ω_s	4T shell vibrational frequency (5.41), (Table 5-1)
$\Omega_n(\vec{r})$	Spatial factor for annular geometry (4.18), (4.33)
∇	Gradient operator
∇^2	Laplacian operator
$\Box^2$	D'Alembertian operator (4.1)
$\partial/\partial n$	Normal derivative (5.5)